

Review

Recent Progress in Biochar-Based Photocatalysts for Wastewater Treatment: Synthesis, Mechanisms, and Applications

Jiali Cui *, Feng Zhang, Hongyan Li, Jianguo Cui, Yatao Ren and Xiaochen Yu

College of Environmental Science and Engineering, Taiyuan University of Technology, Jinzhong 030600, China; zhangfeng@tyut.edu.cn (F.Z.); lihongyan002@tyut.edu.cn (H.L.); cuijianguo@tyut.edu.cn (J.C.); renyatao@163.com (Y.R.); 13603510061@163.com (X.Y.)

* Correspondence: cuijiali@tyut.edu.cn

Received: 31 December 2019; Accepted: 24 January 2020; Published: 4 February 2020



Abstract: Biochar (BC) is a carbon-rich material produced from pyrolysis of biomass. In addition to its low toxicity, environmental compatibility, and low cost, BC has the desired advantages of well-developed mesoporous structure and abundant surface functional groups. In recent years, BC-based photocatalysts (BCPs) have played a significant role in many environmental fields. In this paper, we highlight the current progress and several exciting results of BCPs by focusing on their synthesis, characterization, mechanisms, and applications in wastewater treatment. Details on various preparation methods include sol–gel, hydrothermal/solvothermal, ultrasound, calcination, and in situ methods are summarized and discussed. The underlying mechanisms and the applications of BCPs for different semiconductors are reviewed. Furthermore, some future trends and potentials are outlined.

Keywords: biochar; photocatalyst; wastewater; applications; mechanisms; preparation method

1. Introduction

Photocatalysis has emerged into an efficient and viable technique for purification of wastewater. Various nanoparticles such as TiO_2 , RuO_2 , SiO_2 , ZrO_2 , ZnO , CdS , and ZnS have been used as semiconductor photocatalysts [1]. Despite the excellent functionality, high photostability, and non-toxicity properties, the quick recombination of hole–electron pairs and poor visible-light response limit the photocatalytic performance of semiconductors [2].

To date, considerable attempts have been made to improve the photocatalytic ability using modification of TiO_2 . In the beginning, metal or metal oxides were used to dope TiO_2 to lower the bandgap energy and motivate the visible-light response. However, metal-based doping photocatalysts increase the carrier recombination rate, induce the photocorrosion, secondary pollution and subject to poor thermal stability [3,4]. The high price also hinders its wide application under visible light. In 2001, Asahi [5] first synthesized a non-metal-semiconductor composite by doping nitrogen. Nitrogen can extend the optical absorption spectra of TiO_2 to 500 nm without reducing ultraviolet light. Subsequently, researchers began to study various non-metal-based photocatalysts [6,7]. Doping of semiconductors (e.g., TiO_2 , ZnO , ZrO_2) with non-metals such as C [8], S [9,10], N [11], B [12], F [13,14] and P [15] helped to improve the photocatalytic efficiency. Moreover, non-metals could extend the visible region absorption close to the edge of the valence band, which is more advantageous than metal in improving the visible-light response [16,17].

Among them, combining semiconductors with carbonaceous nanomaterials has been increasingly investigated due to their tunable structural, electrical properties, a wide range of visible-light absorption

and enhanced electronic conductivity [4]. Khan et al. [18] first achieved the doping of carbon in the natural gas flame by heating the Ti metal. It significantly changed the absorption characteristics of the catalyst to visible light. Its photoelectric conversion efficiency can reach 8.35%, compared with that of pure TiO₂ (1.08%). Sakthivel et al. [19] found that the photocatalytic effect of carbon doping was five times higher than that of nitrogen-doped samples. Chen et al. [20] compared the photocatalytic activities of carbon and nitrogen-doped TiO₂ samples under visible-light irradiation. They suggested the higher photocatalytic activity was due to the synergistic effect of carbon and nitrogen atoms. Wang et al. [21] theoretical calculation results demonstrated the forbidden band gap of C-TiO₂ was narrowed down to 2.35 eV. They proposed that the introduction of carbon can narrow the band gap, thus enhancing the photocatalytic performance. However, the widespread application of carbon-based photocatalysts was most limited because of the high price and complicated fabrication methods of these materials. Thus, the development of cheap, sustainable and efficient photocatalysts will be of great interest (Figure 1).

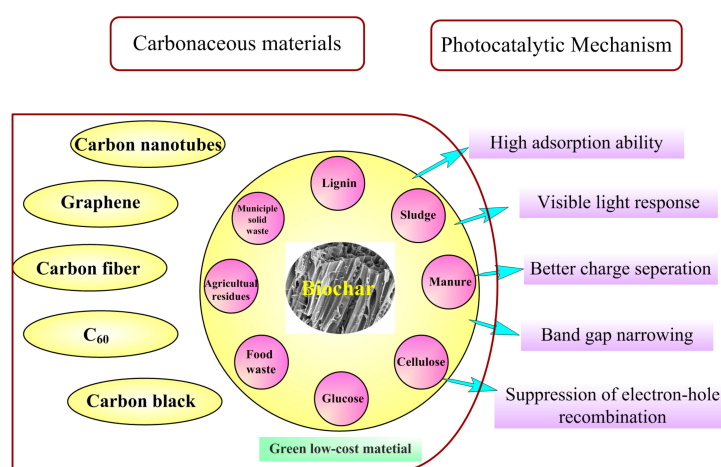


Figure 1. Carbonaceous materials and the mechanisms of BCPs on the treatment of wastewater.

Biochar (BC) is produced through pyrolysis, gasification and hydrothermal carbonization of biomass. The biomass feedstocks include wood materials, forestry products, sludge, manure, agricultural residue and organic wastes. In comparison with most conventional activated carbon, biochar possesses a well-developed mesoporous structure and abundant surface functional groups. Furthermore, it can be served as a versatile catalyst or catalyst support [22]. In recent years, biochar-based photocatalysts (BCPs) have received great attention in various environmental fields [23–27]. Some of those recently reported BCPs were TiO₂-coconut shell [28], TiO₂-*Salvinia molesta* [29], TiO₂-reed straw [30], TiO₂-ramie char [31], TiO₂-corn cob [32], TiO₂-paper sludge and wheat husks [33], TiO₂-bamboo [34,35], ZnO-waste biomass [36], g-C₃N₄/FeVO₄-pinus roxburghii [37], Bi₂O₃-corn cobs [38], TiO₂-walnut shells [39], TiO₂-olive pits and TiO₂-wood shaving [40], TiO₂-wood pellets [41], and TiO₂-plum stones [42], etc.

This review presents the recent development of typical BC-based photocatalysts used for wastewater treatment. Notably, a significant proportion of the review concerns the synthesis, mechanisms and applications of BCPs reported in literature, and provides useful suggestions for novel BCPs in photodegradation of wastewater.

2. Synthesis

The synthesis route for BCPs has great influence on photocatalytic performance. Various efficient methods and approaches have been reported for the synthesis of BCPs (summarized in Table 1), including sol-gel [28–32,43,44], hydrothermal/solvothermal [36,38,39,45–53], ultrasound [40,41,54,55], calcination [34,56–58] and in situ methods [35,59], etc.

Table 1. Synthesis and the application of BCPs.

BCPs	Biomass	Pollutants	Synthesis Route	Working Conditions	Performance	Refs.
BC-TiO ₂	Coconut shell	Reactive Brilliant Blue KN-R	Sol-gel	[KN-R] = 30 mg·L ⁻¹ , [BCPs] = 6 g·L ⁻¹ Ultraviolet (UV) light	99.71% (pH = 1, 60 min) 96.99% (pH = 11, 60 min)	[28]
BC-TiO ₂	Salvinia molesta (SM)	Acid Orange 7 (AO7)	Sol-gel Mechanical mixing	[AO7] = 20 mg·L ⁻¹ , [BCPs] = 0.25 g·L ⁻¹ UV light	57.6% (180 min)	[29]
BC-TiO ₂	Reed straw (RS)	Sulfamethoxazole (SMX)	Sol-gel	[SMX] = 10 mg·L ⁻¹ , [BCPs] = 1.25 g·L ⁻¹ UV light	91.27% (180 min)	[30]
BC-TiO ₂	Ramie char	Safranine T (ST)	Modified sol-gel	[ST] = 500 mg·L ⁻¹ [BCPs] = 2 g·L ⁻¹ UV light	226.7 mg·g ⁻¹ (120 min)	[31]
BC-TiO ₂	Corn cob (CC)	SMX	Sol-gel	[SMX] = 10 mg·L ⁻¹ , [BCPs] = 5 g·L ⁻¹ UV light	91% (removal efficiency, 360 min) 81% (mineralization, 360 min)	[32]
BC-TiO ₂	Sugarcane bagasse	Methyl orange (MO)	Sol-gel	[MO] = 3×10 ⁻⁵ mol/L [BCPs] = 1 g·L ⁻¹ Visible light	95.0% (300 min)	[43]
BC-Zn/TiO ₂	Reed straw	SMX	Modified sol-gel	[SMX] = 10 mg·L ⁻¹ [BCPs] = 1.25 g·L ⁻¹ Visible light	81.21% (180 min)	[44]
BC-ZnO	Waste biomass	Orange G dye (OG)	Hydrothermal	[OG] = 50 mg·L ⁻¹ [BCPs] = 1 g·L ⁻¹ UV and Visible light	88.4% (Visible light) 94.1% (UV light)	[36]
BC-TiO ₂	Walnut shells	MO	Hydrothermal	[MO] = 20 mg·L ⁻¹ , [BCPs] = 0.25 g·L ⁻¹ UV light	92.45% (decolorization, 150 min) 76.56% (mineralization, 150 min)	[39]
BC-Bi ₂ O ₂ CO ₃ / g-C ₃ N ₄ /CoFe ₂ O ₄	Prunus dulcis	Paraquat (PQT)	Hydrothermal	[PQT] = 20 ppm [BCPs] = 0.5 g·L ⁻¹ Visible light and sunlight	99.3% (Visible light, 90 min) 92.1% (Solar light, 120 min)	[45]
BC-TiO ₂	Hazelnut shell (HS) and olive residue (OR)	Methylene blue (MB)	Hydrothermal Sol-gel	[MB] = 10 ppm, [BCPs] = 1g·L ⁻¹ Visible light	96.97% (HS-TiO ₂ , 420 min) 82.52% (OR-TiO ₂ , 420 min)	[46]

Table 1. Cont.

BCPs	Biomass	Pollutants	Synthesis Route	Working Conditions	Performance	Refs.
BC-TiO ₂	Lignin	Acetaminophen (ACE)	Solvothermal	[ACE] = 5 mg·L ⁻¹ [BCPs] = 0.25 g·L ⁻¹ Solar radiation	92% (360 min)	[47]
N-BC-Bi ₂ WO ₆	Pine	RhB, Cr(VI)	Solvothermal	[RhB] = 10 mg·L ⁻¹ [BCPs] = 1g·L ⁻¹ Visible light	99.1% (RhB, 45 min) 96.7% (Cr(VI), 30 min)	[48]
C/Fe ₃ O ₄ /Bi ₂ O ₃	Corn cobs	Tetracycline (TC)	Solvothermal	[TC] = 20 mg·L ⁻¹ [BCPs] = 1g·L ⁻¹ Visible light	91% (90 min)	[38]
BC-Zn-Co-LDH	Wheat husks and paper sludge	Gemifloxacin (GMF)	Hydrothermal	[GMF] = 15–35 mg·L ⁻¹ [BCPs] = 0.15–0.75 g/L UV-B light	92.7% (130 min)	[49]
BC-g-MoS ₂	Rice straw	TC	One-pot hydrothermal	[TC] = 20 mg·L ⁻¹ [BCPs] = 0.4 g·L ⁻¹ Visible light	70% (240 min)	[50]
BC-BiOX(X = Cl, Br)	Biochar	MO	One-step hydrolysis	[MO] = 0.03 mM [BCPs] = 0.6 g·L ⁻¹ Visible light	82% (150 min)	[51]
BC-BiOX(X = Cl, Br)	Sodium carboxymethyl cellulose	TC	One-step hydrolysis	[TC] = 20 mg·L ⁻¹ [BCPs] = 0.25 g·L ⁻¹ Visible light	96.5% (BiOBr-BC), 60 min 60.3% (BiOCl-BC), 60 min	[52]
BC-mp/CdS	Biomass	Rhodamine B (RhB)	Modified hydrothermal	[RhB] = 10 ppm [BCPs] = 0.05g·L ⁻¹ Visible light	$K = 2.7 \times 10^{-2} \text{ min}^{-1}$	[53]
BC-TiO ₂	Olive pits (OP) and wood shaving (WS)	Cr(VI)	Ultrasonic-assisted sol-gel	[Cr(VI)] = 10 ppm [BCPs] = 0.5 g·L ⁻¹ UV and visible light	100% (30 min, 50 min, and 130 min under visible light for AC-TiO ₂ , OP-TiO ₂ and WS-TiO ₂ respectively)	[40]
BC-TiO ₂	Softwood Miscanthus straw	Phenol	Ultrasound-promoted wet impregnation methodology	[Phenol] = 50 ppm [BCPs] = 1g·L ⁻¹ UV and Visible light	64.1% (UV light, 240 min) 33.6% (Visible light, 240 min)	[41]
BC-TiO ₂	Soft Wood Pellets	Phenol	Ultrasound-assisted methodology	[Phenol] = 50 mg·L ⁻¹ [BCPs] = 1g·L ⁻¹ UV and Visible light	42.7% (UV light, 240 min) 15.6% (Visible light, 240 min)	[54]

Table 1. Cont.

BCPs	Biomass	Pollutants	Synthesis Route	Working Conditions	Performance	Refs.
BC-TiO ₂ /CuO	Hemp stems	Ammonia	Sonicated method	[Ammonia] = 100 mg·L ⁻¹ [BCPs] = 1g·L ⁻¹ UV and Visible light	99.7% (UV light) 60.7% (Sunlight)	[55]
BC-Fe ₃ O ₄ /BiVO ₄	Pinus roxburghii	Methylparaben (MeP)	Multiple method	[MeP] = 5 mg·L ⁻¹ [BCPs] = 0.1g·L ⁻¹ Solar radiation	97.4% (120 min)	[60]
BC-g-C ₃ N ₄ /polyaniline/RGO	Bio-waste	Ibuprofen (IBN) 2,4-Dichlorophenoxy acetic acid (2,4-D)	Multi-step thermal treatment method	[IBN] = 20 mg·L ⁻¹ [2,4-D] = 20 mg·L ⁻¹ [BCPs] = 0.5 g·L ⁻¹ Visible light and Natural sunlight	99.7% (2,4-D, 90 min) 98.4% (IBN, 90 min)	[61]
BC-TiO ₂	Softwood/Lignin	Phenol	Mechanical mixing/pyrolysis	[Phenol] = 50 mg·L ⁻¹ [BCPs] = 1 g·L ⁻¹ UV light	52.5% (TiO ₂ -SWP700, 240 min) 35.8% (TiO ₂ -LIGNIN, 240 min)	[62]
BC-TiO ₂	Bamboo	MB	Calcination	[MB] = 12.8 mg·L ⁻¹ [BCPs] = 0.2g·L ⁻¹ UV and Visible light	97% (60 min)	[34]
BC-CdS	Lotus-leaf	RhB, MO, MB	Calcination	[Dye] = 40 mg·L ⁻¹ [BCPs] = 0.1g·L ⁻¹ Visible light	97.8% (MO, 60 min) 96.3% (MB, 150 min)	[56]
BC-g-C ₃ N ₄	Camellia oleifera shells	Cr(VI)	Calcination	[Cr(VI)] = 10 mg·L ⁻¹ [BCPs] = 0.2 g·L ⁻¹ Visible light	100% (240 min)	[57]
BC-ZnO	Corn cob (CC) Red mombin seed (RMS)	MB	Calcination	[MB] = 10 mg·L ⁻¹ [BCPs] = 0.1, 0.2, 0.5 g·L ⁻¹ UV light	K ₁ = 0.09 min ⁻¹ (CC-ZnO, 300 min) K ₁ = 0.06min ⁻¹ (RMS-ZnO, 300 min) 91.12% (Remove efficiency, 60 min)	[58]
BC-CoFe ₂ O ₄ /Ag ₃ PO ₄	Pine pollen	Bisphenol A (BPA)	In situ precipitation	[BPA] = 20 mg·L ⁻¹ [BCPs] = 0.5 g·L ⁻¹ Visible light	80.23% (Mineralization, 60 min)	[59]
BC-CdSe	Bamboo	TC	In situ method	[TC] = 20 mg·L ⁻¹ [BCPs] = 0.5 g·L ⁻¹ Visible light	73% (80 min)	[35]

Table 1. Cont.

BCPs	Biomass	Pollutants	Synthesis Route	Working Conditions	Performance	Refs.
BC-g-C ₃ N ₄ /FeVO ₄	Pinus roxburghii	Methyl paraben (MeP), 2-chlorophenol (2-CP)	Multi-step (thermal treatment, acid treatment, and ammonia treatment)	[MeP/2-CP] = 20 mg·L ⁻¹ [BCPs] = 0.5 g·L ⁻¹ Sunlight	TOC removal rate: 74.2% (MeP, 60 min) 73.9% (2-CP, 60 min)	[37]
BC-TiO ₂	Macroalgae	Simulated textile wastewater (TW)	Wet precipitation	[TW] = 5 mg·L ⁻¹ [BCPs] = 2 g·L ⁻¹ Visible light	99.20% (180 min)	[63]
BC-Bi/Bi ₂ O ₃	Rice straws (RS)	Estrone	Impregnation	[Estrone] = 2.8 mg·L ⁻¹ [BCPs] = 1 g·L ⁻¹ UV and Visible light	K _{obs} = 0.045 min ⁻¹ (60 min)	[64]

2.1. Sol-gel Method

The sol-gel method is relatively simple, and the prepared nanomaterials have high purity and uniform particle size. Generally, the sol is prepared by uniformly mixing the sol and the carbon materials, followed by ageing to form a gel and calcination at a higher temperature. However, the main disadvantage of this method is the shape of the material is not well controlled.

Recently, Zhang et al. [28] fabricated BC(coconut shell)-TiO₂ compound by sol-gel method. First, the coconut shell was pyrolyzed under nitrogen, followed by washing and rinsing with HCl acid. Secondly, the acid-treated biochar was ageing, washed, dried overnight, and sieved through the mesh. Then, the sol-gel process involved the following sequences. (1) Mixed ethanol with butyl titanate to form solution A; (2) solution B was obtained through mixing ethanol, deionized water, acetic acid with polyethylene glycol; (3) dropwise added solution B into solution A and aged for 24 h. Then, the as-prepared BC was mixed with the sol-gel. Finally, the above mixture was further treated by ageing, filtration, drying, and calcination to form the BCPs. The scheme of the BCPs synthetic process was illustrated in Figure 2A.

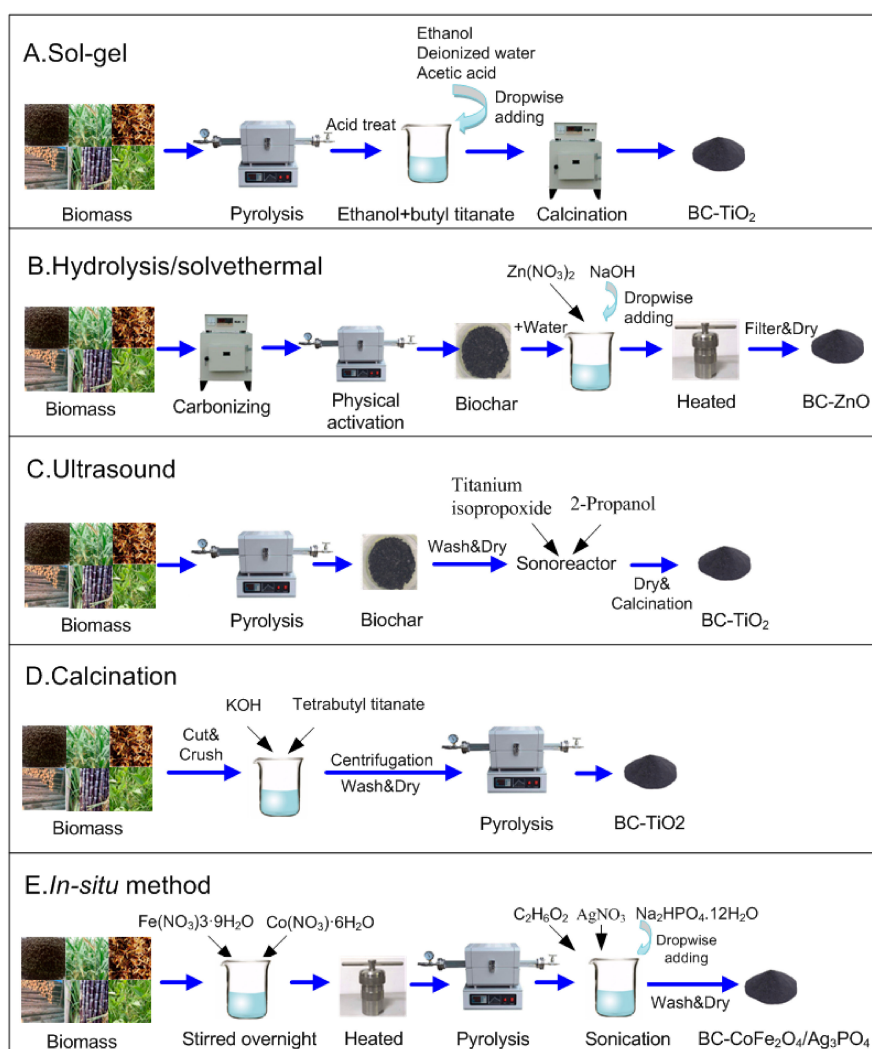


Figure 2. Schematic image of the preparation methods of BCPs.

For comparison, Silvestri et al. [29] impregnated TiO₂ in the *Salvinia molesta* derived carbonaceous matrices via the sol-gel process and mechanical mixing route. The results showed that the type of TiO₂ precursor plays a much more critical role than the impregnation method on the photocatalytic

efficiency of the composites. Compared with the sol–gel way, the BCPs fabricated by mechanical mixing exhibited higher photocatalytic performance.

2.2. Hydrothermal/Solvothermal Method

Hydrothermal/solvothermal method is a crystallization process at relatively low reaction temperature ($< 200\text{ }^{\circ}\text{C}$) and higher pressure. It has gained plenty of successes for its outstanding advantages of low agglomeration, better product purity, higher dispersion and low cost in energy [65]. Different kinds of BCPs can be attained by the hydrothermal/solvothermal technique [36,45–53].

Vinayagam et al. [36] synthesized ZnO/BC composite by hydrothermal method (shown in Figure 2B). In a typical synthesis, waste biomass was washed and dried, followed by carbonizing under $500\text{--}600\text{ }^{\circ}\text{C}$. Then, the obtained material was activated via physical activation method under an inert atmosphere. Different weight ratios of BCPs were prepared. First, zinc nitrate and BC were mixed and stirred in distilled water, followed by dropwise adding NaOH (1 M) till the pH was 10. Then, the suspension was heated for 6 h at $120\text{ }^{\circ}\text{C}$. Later, the obtained material was centrifuged, washed, and dried overnight. The result showed ZnO exhibited reduced band gap energy, excellent activities, and reusability either under UV or visible-light irradiations by combined with BC.

In another study, Peñas-Garzón et al. [47] prepared TiO_2/BC composite for photocatalytic degradation of acetaminophen under solar light via a multi-step solvothermal process. First, the biomass (lignin) was activated by using different agents. Then, the BC was suspended into the EtOH at room temperature to form solution A. Meanwhile, $\text{Ti}(\text{OBU})_4$ was diluted into EtOH (solution B). Later, solution B was dropwise added to solution A until complete homogenization. Afterwards, the hydrolysis of the Ti precursor was performed by adding dropwise water. The mixture was stirred and heated, followed by separation, washing, and drying overnight to obtain TiO_2/BC . Through hydrothermal/solvothermal route, anatase phase with an average grain size of 10 nm was formed. $\text{TiO}_2\text{-BC}$ displayed much higher activities than bare TiO_2 for the removal of acetaminophen under solar light.

2.3. Ultrasound Method

Ultrasound method has rapidly attracted considerable attention in recent years. As a green technology, this procedure has excellent potential for photocatalysts fabrication, owing to the low temperature, atmospheric pressure, and instant reaction. The obtained photocatalyst exhibited purity phase, high surface area, uniform particle coatings, and different particle sizes and shapes. Moreover, the parameters can be easily adjusted in the preparation process [66]. Lisowski's group [41,54,66] have developed a series of $\text{TiO}_2\text{-BCPs}$ derived from biomass via a novel ultrasound-assisted methodology. The typical preparation procedure was as follows (Figure 2C). Biochar was prepared via pyrolysis of softwood pellets and miscanthus straw pellets. Then, the as-fabricated BC was mixed with titanium isopropoxide and 2-Propanol, followed by sonication for 1 h. Later, the solvent was removed using a rotary vacuum evaporator assisted by sonication. Subsequently, the obtained mixture was dried and calcined at $400\text{ }^{\circ}\text{C}$ in static air to obtain BCPs. The authors demonstrated that ultrasound could promote the formation of C-C sp^2 and sp^3 , C-O-C, COOH, O=CO and C=C-OH, which may lead to the evolution of surface oxygen vacancies and Ti^{3+} defects.

2.4. Calcination

Wang et al. [34] fabricated bamboo char- TiO_2 composites by calcination route. The schematic for the calcination process is given in Figure 2D. Typically, the bamboo was cut and crushed into powder with different sizes. Then, the bamboo power and tetrabutyl titanate were added into the potassium hydroxide (KOH) solution and kept stirring, followed by centrifugation, washing and drying. Afterwards, the obtained precursors were calcinated at $800\text{ }^{\circ}\text{C}$ under inert gas. They suggested that through the calcination method, the crystallinity of the BCPs was enhanced (93.2%), compared

with that of precursor (78.3%). The BCPs improved the photocatalytic activity under both visible-light irradiation and UV region.

In another research, biochar (camellia oleifera shells) coupled g-C₃N₄ nanosheets composites were prepared by a two-step calcination method by Li et al. [60]. They found that the double calcination process can promote the removal of the small g-C₃N₄. Moreover, owing to the synergistic effects, the BCPs displayed remarkable stability for 4-FP degradation.

2.5. In-Situ Method

Carbon doped anatase TiO₂ spheres can be prepared via an in situ method, which was considered to avoid the aggregation of carbon species arises in external carbon precursors addition. Furthermore, carbon can dope in the place of oxygen in the TiO₂ lattice [4]. Some researchers [35,62,63,67] have reported the synthesis of BCPs using the in situ method. Brandes et al. [67] proposed an in situ approach to insert TiO₂ in the bacterial cellulose matrix. Typically, bacterial cellulose hydrogel was suspended in H₂SO₄ solution (65%), followed by dropwise addition of TiOSO₄·H₂SO₄·H₂O and constant stirring. Then, the mixture was filtered, washed, and dried under vacuum to obtain the BCPs. The ex situ method was also employed for comparison. Spherical bacterial cellulose hydrogels were mixed with P25 and deionized water, forming a sol-gel solution. Afterwards, the as-fabricated mixture was stirred, separated, and washed to remove the residues for further use. They found that the MB removal rate of 70.83 % and 89.58 % were achieved, through in situ and ex situ route, respectively.

Very recently, Zhai et al. [62] synthesized BCPs via an in situ precipitation method (Figure 2E). The magnetic BC@CoFe₂O₄ was fabricated by a one-pot method. Pine pollen was mixed with Fe(NO₃)₃·9H₂O and Co(NO₃)₆·6H₂O and stirred overnight, followed by pH adjusting till 12 with NaOH and stirring another 1 h. Then, the obtained solution was heated at 180 °C for 12 h. Later, the as-prepared powder was pyrolyzed at 500 °C under nitrogen atmosphere to obtain the magnetic biochar (BC@CoFe₂O₄). BC@CoFe₂O₄/Ag₃PO₄ was further synthesized via the in situ precipitation method. BC@CoFe₂O₄ were added to C₂H₆O₂ and sonicated for 30 min, followed by adding 50 mL AgNO₃. Then, 50 mL Na₂HPO₄·12H₂O was dropwise added to the above mixture and kept stirring. Later, the as-prepared mixture was washed and collected for further use. They demonstrated that the increased photocatalytic performance for bisphenol A removal was owing to the in situ process.

3. Characterization

Various characterization methods have been carried out to evaluate the physical, chemical, and mechanical properties of BC and BCPs, such as scanning electron microscopy (SEM), scanning electron microscopy-energy dispersive X-ray spectrometry (SEM-EDS), transmission electron microscopy (TEM), X-ray diffraction (XRD), Fourier transform infrared (FT-IR), Raman spectroscopy, X-ray photoelectron spectroscopy (XPS) and solid-state nuclear magnetic resonance (NMR), etc. (Figure 3).

3.1. Morphology and Surface Area

SEM provides information regarding the structure and microscopic features of BC and BCPs. The sizes of the pores in the BC may be different extremely as the pyrolysis temperature increased. For example, the BC present honeycomb-like pores at a pyrolysis temperature of 700 °C while it disappeared at 200 °C [68]. However, the hollow structure of BC may be broken when the pyrolysis temperature increased to 700 °C [55]. TEM is exceptional for its quality to identify the morphology, crystallinity, and structure of BC and BCPs. Abdul et al. [69] found that graphene nanosheets were transparent and slightly aggregated within BC through the TEM images. Xiao et al. [70] observed the multi-layered structures and nanocrystalline structures of BC.

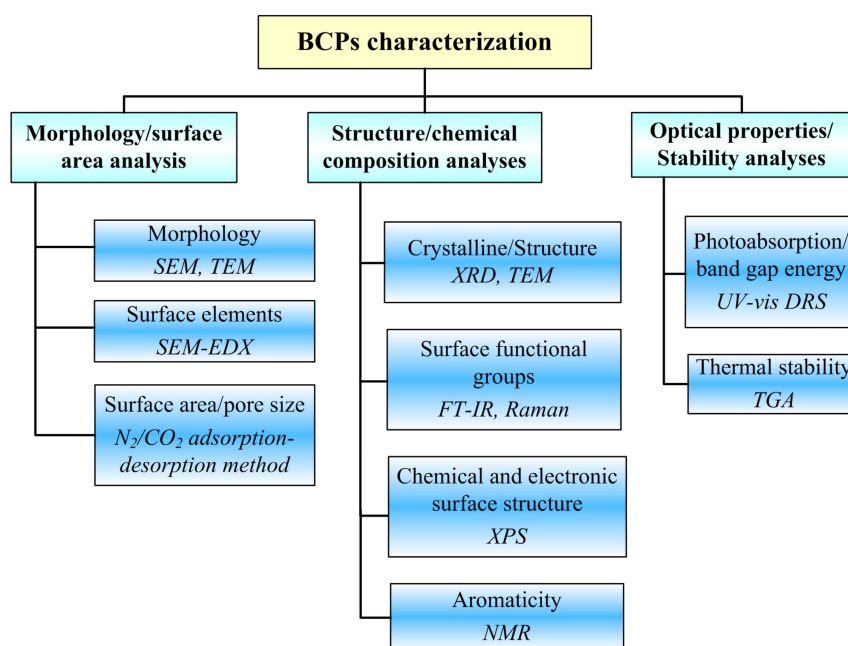


Figure 3. Graphical overview of BC and BCPs characterization.

SEM-EDS is widely applied to identify and quantify the elements in BC. For instance, it was observed that the predominant elements in the sludge-derived BC samples were carbon, oxygen, silica, aluminum, calcium, sulfur, phosphorus, and potassium, etc. [71]. Zhao et al. [68] used SEM-EDS to analyze the elements in the rapeseed stem biochar. They demonstrated the C content increased, and the O content decreased as the pyrolysis temperature rose.

The specific surface areas (S_{BET}) and porosity properties of the BC and BCPs could be investigated by N_2 adsorption-desorption isotherm. Generally, the large specific surface area facilitates the adsorption of pollutants. In most cases, after the combination, the S_{BET} of the BCPs is higher than that of the original BC. However, it was found that the mesopores and micropores of BC may be clogged due to the aggregation of semiconductors, thus inducing the decrease of the S_{BET} [62,72].

3.2. Structure and Chemical Composition

XRD is frequently applied to examine the crystalline structure and phase of BC and BCPs. Ye et al. [50] compared the XRD spectrum before and after catalytic degradation. They found that the crystal structure of the g-MoS₂/PGBC remains unchanged. Fazal et al. [63] used XRD to investigate the BC (macroalgae) and BC-TiO₂ composite. XRD spectra showed that the peak located at 26.9° and 43° corresponded to the (002) plane of crystalline carbon, associating with the graphite-like structures. Furthermore, the graphitic peaks declined with the increase of TiO₂ loading, indicating the good intercalation of TiO₂ nanoparticles between BC layers.

FT-IR spectra can be applied to distinguish the functional groups and the degree of carbonization of BC. The band absorbance at 710 cm^{-1} was a characteristic feature of BC [63]. The peak between 875-1035 cm^{-1} was associated with C–O and OH– stretching vibration. The absorption band was found to shift to higher wavenumber with the increase of TiO₂, which indicated that the T–OC– bond changed the optical property and charge transfer. Geng et al. [73] used FT-IR spectra to investigate the molecular component and the degree of carbonization of BC (cellulose). The peaks at 3450, 1750, 1635 and 1040 cm^{-1} can be assigned to the stretching vibration of the –OH, C=O and C–O–C, respectively. It was stated that the cellulose skeleton was converted to the graphitic structure of amorphous carbon nanofibers during the pyrolysis process.

XPS measurement is applied to analyze the composition and surface chemistry of BC and BCPs. More functional groups of BC at binding energies of 291.2 eV and 531.8 eV associated with carbonates

and C=O were observed than in the case of pure lignin [62]. It was found that the pyrolysis process can cause an increase in the surface activity of carbon functional groups present on the surface of BC. Moreover, binding energies of 284.8 eV and 288.6 eV were due to the adventitious elemental carbon and C–O bonds, respectively, indicating the presence of Ti–O–C structure [74].

Raman spectroscopy can be used to characterize BC-based nanostructures. Al-Kahtani et al. [75] demonstrated the D band at 1351 cm^{-1} and G band at 1587 cm^{-1} was characteristic bands of graphite carbon. The intensity ratio (I_D/I_G) reflected the crystalline and graphitization of BC [38]. The I_D/I_G value of C/Fe₃O₄/Bi₂O₃ and C/Fe₃O₄ were 0.84 and 0.82, respectively, indicating that the graphitization of BC made the BCPs from disorder to order, which was beneficial for electronic conduction. Lower I_D/I_G means higher graphitization. The BCPs fabricated via ultrasound route displayed a slightly lower I_D/I_G value (0.37) compared to pure BC (0.48). It was stated the slight change of graphitization might be caused by the reconstruction of structural defects within the sp² carbon network that arose upon the ultrasound-assisted synthesis method [41].

NMR is another spectroscopic technique commonly used to in-depth investigate the fine structure of BC. The degree of carbonization and stability of BC pyrolyzed at different temperatures and heating rates can be compared using the NMR spectroscopy [76,77]. Moreover, it can provide details on the functional groups and hydrocarbons [78]. Moreover, it was considered that NMR was more suitable for analyzing BC containing C compounds than functional groups [79]. Hence, researchers commonly used both NMR and FT-IR to examine the structure and functional groups.

3.3. Optical Property and Stability

UV–vis diffuse reflectance spectroscopy (DRS) is commonly applied to investigate the optical properties and energy band features of BCPs. Carbon can expand the absorbance range to the visible region [74]. The BCPs showed a red-shift toward longer wavelengths when semiconductors were combined with BC to form the composites [40,41]. However, the absorbance was relatively weak in the visible region because of the low content of BC [43]. The band gap energy of BCPs can be calculated by application of the Kubelka–Munk function [36,80]. The BCPs displayed much different photocatalytic performance in terms of the difference in band gap energy values [41].

Thermogravimetric analysis (TGA) is performed to assess the mass loss and relative stability of BC. Xiong et al. [81] applied TGA to analyze the thermal stability of sulfonated BC. The derivative thermogravimetric (DTG) peak at 600–700 °C diminished while the peak at 200–300 °C became predominant after the sulfonation process. At 1000 °C, the TGA spectra exhibited a more significant mass loss of sulfonated BC (20 wt.%), in comparison with raw BC (16 wt.%), indicating that sulfonation inevitably weakened the thermal stability of BC.

4. Mechanism

Semiconductors have been widely studied for its high thermal and chemical stability, strong oxidizing ability and low cost. Owing to the relatively wide band gap energy (3.20 eV) and low quantum efficiency, TiO₂ can only respond in the ultraviolet light, which occupies only about 5% of the sunlight spectrum. Therefore, the development of photocatalysts for absorbing visible light is highly required. The participation of biochar in the synthesis process can change the structure, morphology and light absorption efficiency of the composites, leading to an enhanced performance. The functional groups existed in the biochar may also play pivotal roles in the reaction and further promote the photocatalytic ability [52]. Contaminants in wastewater can be removed based on different mechanisms, which involve: adsorption ability, narrowing the band gap, facilitating the electron transport, suppression of electron/hole charges recombination, π - π stacking interactions, electrostatic interaction, reducing the photocorrosion of TiO₂, etc. The main mechanisms are summarized below.

4.1. Adsorption

Owing to its large surface areas, structure stability, and low cost, BC has been frequently applied as support to disperse catalyst nanoparticles. Impregnation of foreign materials onto BC can remove various contaminants through simultaneous adsorption and degradation. In this integrated technology, the adsorption process can enrich pollutants to facilitate the degradation process, as free radicals are very short lived [82]. Kumar et al. [60] concluded that the adsorbed contaminants were more prone to attack by radicals. As soon as the methylparaben was adsorbed onto the surface of BC, it got degraded. Ye et al. [50] explored the removal of tetracycline hydrochloride was dependent on adsorption and degradation processes. They found the BCPs displayed comparatively large adsorbed ability, which was enhanced with increasing BC content. Moreover, the BCPs exhibited a better adsorption effect but weak photocatalytic degradation performance, owing to the poor electron conductivity of the inactivated BC and the serious stacking of MoS₂. BC can be used as support structure for adsorption molecules and as potent substrate for the growth of TiO₂ photocatalyst on its functionalized surface [63].

4.2. Narrowing the Band Gap

Combining TiO₂ with carbonaceous nanomaterials may result in the band gap narrowing. Some ways were summarized below.

(i) Ti-O-C bonding bridge. Di Valentin et al. [83] investigated that carbon can act as a dopant to replace O and Ti by using density functional theory (DFT) calculations. The calculated structures suggested it was easier to replace O when the amount of doped carbon is low and in the oxygen-poor environment, whereas, under oxygen-rich condition, substitution to Ti is preferred. The chemically bonded Ti-O-C plays a significant role in narrowing the band gap, thus promoting the photocatalytic ability [84–86]. The spectral response range can be broadened to the visible region due to the forming of Ti-O-C bonds [87,88]. Djellabi et al. [89] synthesized TiO₂-olive pits lignocellulosic biochar photocatalysts via ultrasonic-assisted sol-gel method. TiO₂ clusters were successfully bonded to BC functional groups through Ti-O-C bridge (Figure 4A). The Ti-O-C was more pronounced in the samples of lower BC content, while the light absorbance increased with the BC content. Additionally, the optical absorption edge of TiO₂ was shifted towards the visible-light region due to the introduction of BC. Ti-O-C bonds exhibited a remarkable role in band gap narrowing. The band gap energy varied from 3.02 to 2.63 eV depending on the TiO₂/BC ratio.

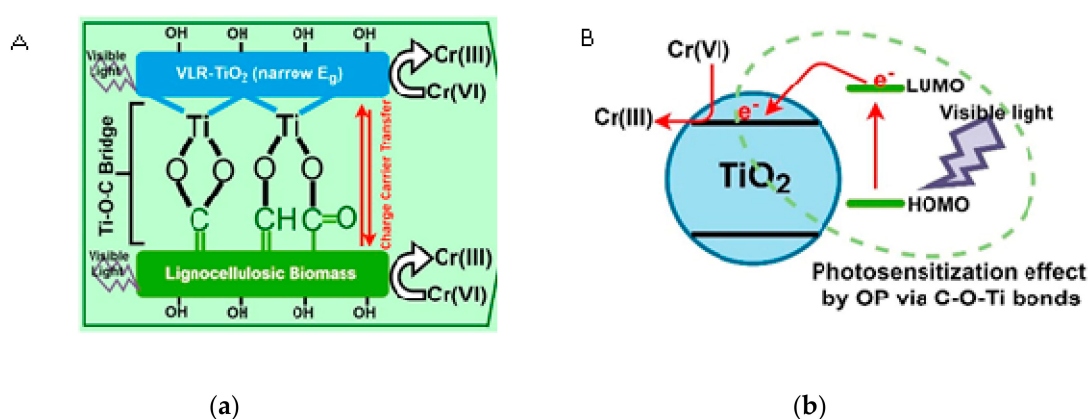


Figure 4. Schematic illustration of the proposed mechanism of narrowing the band gap induced by C-O-Ti bond (A) and photosensitization (B). Reproduced with permission from reference [89].

(ii) Carbonaceous materials can act as photosensitizers and charges receiver to narrow the band gap when combined with other semiconductors [89,90]. Djellabi et al. [89] demonstrated that the BC displayed an organic structure, which induced the visible-light absorption. The photosensitization of TiO₂ by BC polymer is shown in Figure 4B. Although the BCPs with higher biochar content showed an

obvious visible-light response and narrow band gap, the photocatalytic reduction rate of Cr(VI) was the lowest. It was because the higher content of biochar may block the light absorption and affect the electrons generating. Peng et al. [55] reported similar photosensitization effects by BCPs.

4.3. Facilitating the Electron Transport

By introducing of biochar, the separation efficiency of electron-holes is enhanced due to the excellent electron transmission ability [91], thus significantly improved charge transport properties. Meng et al. [92] stated that the π -conjugated electron systems from BC was an efficient electronic transfer. The h^+ migrates to the surface of TiO_2 and produce $\cdot OH$, which prolonged the separation lifetime of e^- and h^+ [30]. BC modified Z-scheme heterojunction was constructed via a facile method [93] (Figure 5). The BCPs showed excellent photocatalytic activity of tetracycline (TC) and Cr(VI), recyclability and stability. $\cdot O_2^-$, $\cdot OH$ and h^+ generated in the photodegradation process were proved to be the important active species. Much higher $\cdot O_2^-$ generated in BCPs mainly attributed to the electrons transferred from the conduction band of $g-C_3N_4$ to the surface of BC. BC decorated Z-scheme system effectively facilitated the interfacial charge separation and transfer (Figure 3). Li et al. [51] prepared BC/BiOX (X = Cl, Br) composites for MO removal. Similarly, they found that as a carbon dopant, the BC can facilitate the charge separation of the BCPs and elevate the photocatalytic performance under visible light.

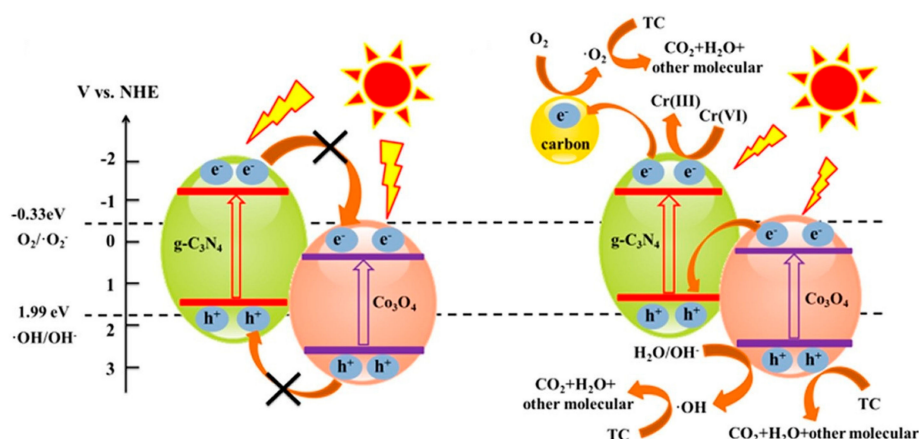


Figure 5. Schematic illustration of the proposed mechanism for facilitating electron transport. Reproduced with permission from reference [93].

4.4. Suppression of Electron-hole Recombination

The lifetime of photogenerated carriers affects photocatalysis significantly. The trapped e^- and h^+ transferred immediately to the surface and reacted with adsorbed oxygen and water molecules to generate free radicals. However, the lifetime is generally nanosecond, and the electron-hole pairs recombine instantly and induce deactivation.

Carbonaceous materials enhance the electrons-holes separation owing to the excellent double conductivity. Peng et al. [55] prepared TiO_2 -CuO/BC (hemp stem) under different calcination temperature (500, 600 and 700°C). They found the enhanced removal of ammonia was owing to the retardation of e^-/h^+ pairs. Moreover, the BC formed a mid-gap energy state above the VB of TiO_2 (Figure 6A). Gao et al. [38] synthesized BC/ Fe_3O_4 / Bi_2O_3 composite via a solvothermal method. The electrons in Bi_2O_3 were transported to the BC/ Fe_3O_4 , thus inhibiting the recombination of h^+ and e^- pairs. The magnetic nanoparticles (BC/ Fe_3O_4) acted as an electron storage center, which was beneficial to transfer the electron from Bi_2O_3 and reduce the probability of electron return to Bi_2O_3 (Figure 6B). Meng et al. [92] suggested the synergistic effect between biochar and $g-C_3N_4$ resulted in a longer lifetime of excited electrons of semiconductor and hindered photo-induced electron-hole recombination. Fazal et al. [63] also found that photodegradation was sensitive to the loading concentration of TiO_2 onto

biochar. The photodegradation efficiency was enhanced owing to the reduced charge recombination. Zhu et al. [91] fabricated biochar-based g-C₃N₄ for 2-Mercaptobenzothiazole degradation. They proposed that the introduction of biochar can produce more active sites and result in highly efficient of electron-hole pairs separation. Furthermore, BC can significantly inhibit the g-C₃N₄ reunion and stacking.

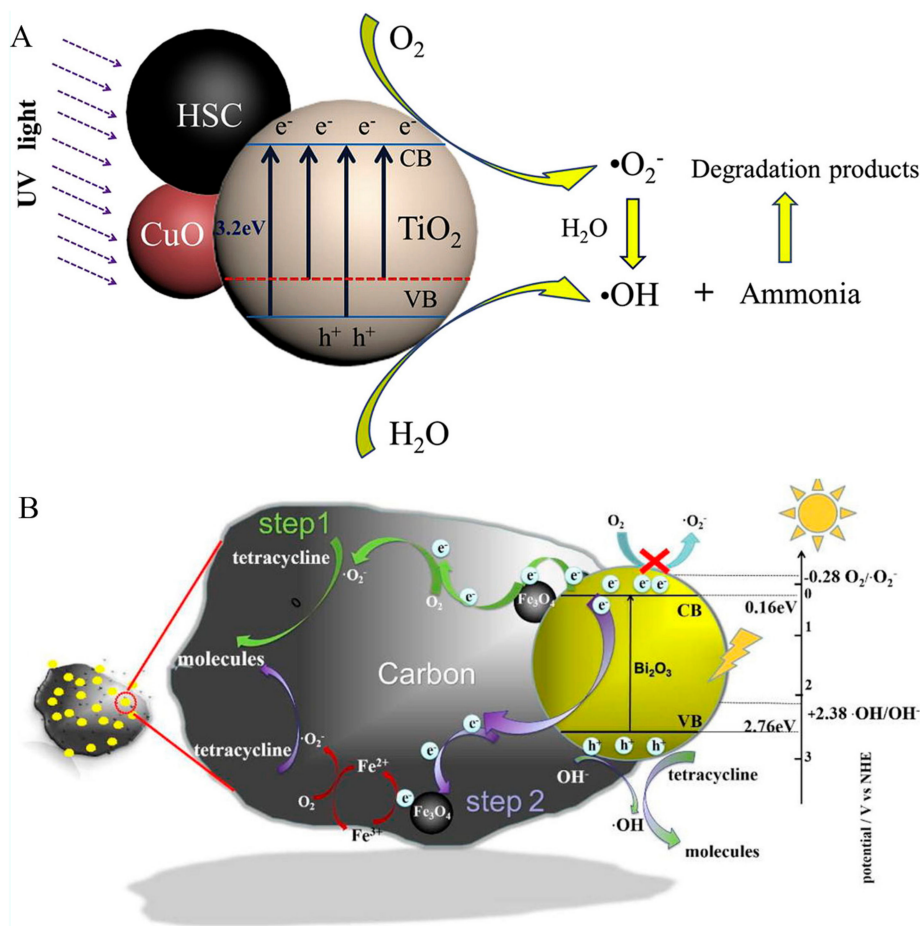


Figure 6. Schematic representation mechanism of suppression of electron-hole recombination. Reproduced with permission from reference [55] (A) and reference [38] (B).

4.5. Others

Besides the above-discussed mechanisms, some other effects of biochar were also proposed. Shi et al. [94] prepared TiO₂/BC (carbonaceous aerogel) composite through a one-pot hydrothermal process. Compared with P25, the composite exhibited excellent photocatalytic activity in MB and CIP degradation under visible-light irradiation. They suggested BC can not only separate the e⁻/h⁺ pairs, but also reduce the photocorrosion of TiO₂. As the main active species, the •OH and •O₂⁻ radicals promoted the photocatalytic activity. The free radicals present in the matrix could induce •OH be trapped by oxygen to form superoxide radical anion [95]. Tan et al. [27,96] summarized the interactions between the organic contaminants and BC, including hydrogen bonding, electrostatic attraction, and ion-exchange in the adsorption process. Fang et al. [97] systematically explored the effects of BC on the transport and transformation of organic contaminants in aquatic systems. It was verified that BC particles could generate ROS, such as •OH and ¹O₂ through BC matrix (BCM) and dissolved organic matter (DOM), thus inducing diethyl phthalate degradation under both UV and solar light.

5. Applications of BC-based Photocatalysts

As a kind of sustainable, low-cost, and environment-friendly material, biochar showed a great of advantages when combined with other semiconductors. The microporous structure and large surface area of BCPs was rewarding for efficient diffusion of reactant to the catalytic sites [98]. Moreover, it enhanced the photodegradation ability for various organic substances (phenanthrene [99], phenol [100] and polycyclic aromatic hydrocarbons [101]) and inorganic substances (hexavalent chromium, total chromium [60] and ammonia [55]). As a carbon-rich material, biochar is beneficial for the formation of hierarchical structure carbonaceous nanomaterials, which possesses the advantage of abundant surface functional groups (sulfonyl groups, phenolic groups, acid complexes, etc.). BC serves as alternative carbonaceous nanomaterials, including carbon nanotubes, graphite, C₆₀, carbon fiber, and g-C₃N₄, etc. [49]. The persistent free radicals contained in biochar can induce the generation of ·O₂ in the presence of oxygen, which will improve the photocatalytic performance [95]. The applications of various BCPs are summarized in Table 1.

5.1. TiO₂-BCPs

During recent decades, TiO₂ has been the most used photocatalyst in the field of water purification owing to the advantages of high photo-activity, price moderate, non-toxicity, low cost and good chemical stability [102]. However, pristine TiO₂ still suffers from the low response of visible light and high charge recombination. In recent years, biochar modified TiO₂ composites (BC-TiO₂) have attracted great attention due to the physical adsorption, electrostatic interaction and suppression of electron/hole charges recombination granted by BC.

Zhang et al. [30] synthesized reed straw biochar-based TiO₂ by sol-gel method. The coupling of TiO₂ and BC suppressed the recombination of e⁻/h⁺ pairs and further promoted photocatalytic degradation efficiency. The sulfamethoxazole removal rate was 91.27%, compared with that of pure TiO₂ (58.47%). Furthermore, the obtained BC-TiO₂ were successfully applied in real water with a removal rate of 65.70%. Very recently, Lu et al. [39] fabricated a series of BC-TiO₂ photocatalysts by direct hydrolysis method and pyrolysis of waste walnut shells for the removal of methyl orange. It showed that catalyst with the weight ratio of 0.2/1 (BC/Ti) exhibited the best decolorization efficiency of 92.45% and mineralization efficiency of 76.56 % after recycling 5 times. Lisowski et al. [41] prepared TiO₂-based wood and straw-derived biochar photocatalysts via an ultrasound-assisted route. The prepared composite pyrolyzed at the temperature of 700 °C had plate-like particles structure, which was beneficial for light use and electron-hole separation. Through Kubelka–Munk function, the band gap energy (E_g) of TiO₂-BC varied from 2.12 to 2.50 eV depending on different biomass feedstocks and temperatures. At the same time, the red-shift in absorption edge of BCPs was observed (Figure 7). They suggested the improved photoabsorption performance and the extended absorption edge was attributed to the introduction of biochar as well as the intimate interfacial contact caused by ultrasound procedure.

5.2. g-C₃N₄-BCPs

The graphitic carbon nitride (g-C₃N₄) has elicited ripples in recent years since Wang et al. [103] discovered the hydrogen production from water over g-C₃N₄ in 2009. g-C₃N₄ processes high physicochemical stability, non-toxic, and unique graphene-like two-dimensional structure. During recent decades, lots of research on BC-g-C₃N₄ conjunctions has been reported.

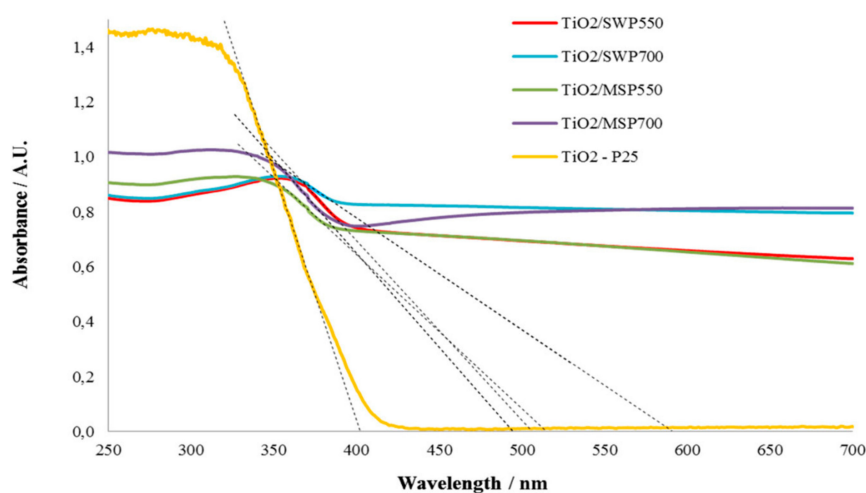


Figure 7. UV-visible diffuse reflectance spectra of BC-TiO₂. Reproduced with permission from reference [41].

Xie et al. [104] summarized the g-C₃N₄-based photocatalysts. The Schottky-junction between g-C₃N₄ and the highly conductive carbon materials enhanced charge separation. Kumar and his co-workers [37,57,105] synthesized a series of BC-based g-C₃N₄ photocatalysts for wastewater treatment. For example, BC supported g-C₃N₄/FeVO₄ were prepared for methylparaben and 2-chlorophenol photodegradation under solar light [37]. The BCPs exhibited excellent photocatalytic activity with the removal rate of 98.4% (methylparaben) and 90.7% (2-chlorophenol), due to the extended solar light response and enhanced charge separation. Recently, Kumar et al. [45] synthesized BC-based g-C₃N₄/Bi₂O₂CO₃/CoFe₂O₄ heterojunction. The high pesticide paraquat removal rate of 99.3% was reached under visible radiation, compared with that of 92.1% under solar light. Due to the greater absorption of the visible spectrum, BC elevated the quantum efficiency, charge separation, and generation of free radicals. Zheng et al. [72] synthesized BC-based g-C₃N₄ via one-pot pyrolysis with different mass ratio. g-C₃N₄ modification can expand biochar's capacity. BC100 (100 (urea): 1 (biomass)) showed 100% removal rate of RR120 through both adsorption and photocatalytic degradation under natural conditions. Li et al. [60] fabricated BC coupled g-C₃N₄ nanosheets composites through two-step calcination strategy to remove the Cr (VI) from wastewater. Graphitized BCPs could completely degrade the Cr(VI) and total Cr, owing to the photogenerated electrons, high thermal stability, and large specific surface area. Zhang et al. [106] synthesized BC modified graphitic carbon nitride via pyrolysis of kapok fiber. The BCPs presented a narrow band gap and extended light absorption. The BC facilitated the electron transfer and improved the photocatalytic activity. It played a center role as the carbon source and substrate in the epitaxial growth of graphitic carbon nitride.

5.3. Bismuth-BCPs

Bismuth-based photocatalyst has attracted considerable interest in wastewater treatment for its excellent photo-oxidation ability, unique electronic structure and toxic-free properties [107]. Very recently, Zhu et al. [64] prepared bismuth impregnated biochar composites for efficient estrone degradation. They found the K_{obs} was more than 20 times than that of pristine Bi/Bi₂O₃. The promoted result was owing to the ·OH radicals generated through the synergistic effect between BC and Bi/Bi₂O₃. Li et al. [107] synthesized Bi₂O₃/ZnAl-LDH-BC composite, which displayed an excellent performance in photocatalytic degradation of contaminations under visible light. Owing to the synergistic effects between precursors, the E_g of the BCPs was lower (2.42), compared with Bi₂O₃ and ZnAl-LDH (2.75 and 2.9, respectively). It was found that the light absorption and the separation of e⁻/h⁺ pairs was expedited. Moreover, organic contaminants include afranine T, brilliant green, RB and 4-nitrophenol exhibited optimal stability (Figure 8). The BCPs hold great potential in the field of wastewater treatment.

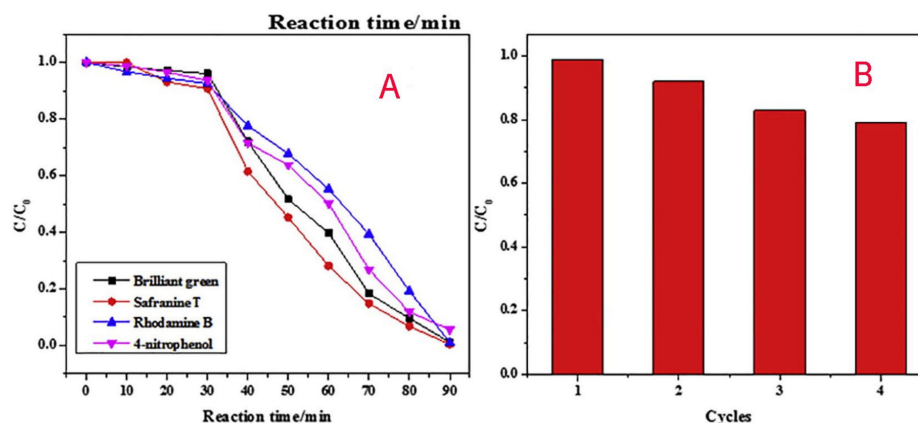


Figure 8. (A) Removal of different organic pollutants over $\text{Bi}_2\text{O}_3/\text{ZnAl-LDH-BC}$, (B) Photocatalysts stability. Reproduced with permission from Ref. [107].

Kumar et al. [60]'s research showed 97.4% of methylparaben was removed in 2 h under natural sunlight by $\text{BC-Fe}_3\text{O}_4\text{-BiVO}_4$ composite. The introduction of BC brings high surface area, which facilitated the degradation via radical attack and expedited the radical generation. Gao et al. [38] synthesized $\text{BC/Fe}_3\text{O}_4/\text{Bi}_2\text{O}_3$ photocatalyst using corn cobs char. Compared with pure Bi_2O_3 , BC and $\text{BC/Fe}_3\text{O}_4$ showed notable red-shift and a broad absorption region. The degradation rate of tetracycline by $\text{BC/Fe}_3\text{O}_4/\text{Bi}_2\text{O}_3\text{-10}$ was 2.5 times greater than the bare Bi_2O_3 . Li et al. [108] found that the increased visible-light absorption was owing to the unique biochar-based heterojunction structure. Bismuth oxyhalides (BiOX) exhibited higher photocatalytic activity than anatase TiO_2 due to its unique layered structure interleaved with $[\text{Bi}_2\text{O}_2]$ slabs and double halogen atoms slabs [51]. Li et al. [109] fabricated a magnetic $\text{Fe}_3\text{O}_4/\text{BiOBr/BC}$ (reed straw) composite with the visible-light response via a one-step hydrolysis route. The BCPs exhibited better photocatalytic activity for carbamazepine removal (95.51%), owing to the promoted separation of e^-/h^+ pairs.

5.4. Carbon Quantum Dots (CQDs)-BCPs

Carbon quantum dots (CQDs) have emerged as a potential alternative to traditional expensive and unsustainable material [110]. It processes the advantages of high biocompatibility, tunability and stability [111]. The electron transfer, photoluminescence, and electron reservoir properties of the CQDs can enhance the structural stability and photocatalytic activity. Briscoe et al. [110] proposed the preparation method of CQDs mainly includes top-down and bottom-up route. In the top-down way, larger carbon structures are broken into smaller fractions. In contrast, the bottom-up approach involves forming the CQDs from molecular precursors. When biomass precursors are used for the production of CQDs, the latter method exhibited the advantages of sustainability and biocompatibility.

The introduction of biochar-based CQDs (BCQDs) to the semiconductor could lead to the change of band structure and extend the light absorption [112]. Yao et al. [80] prepared BCQDs modified flower-like BiOI composite through the solvothermal method. They found $\cdot\text{O}_2^-$ and h^+ was the main active species for MB photodegradation. The BCQDs acted as electron acceptors and further facilitated the separation of electron-hole pairs. Recently, Wang et al. [113] prepared BCQDs and $\text{BCQDs/Ag/Bi}_4\text{Ti}_3\text{O}_{12}$ using hydrothermal treatment of bamboo powder. They suggested the introduction of BCQDs facilitated the photoelectron generation and transport. Furthermore, the BCQDs acted as an electron reservoir and boosted the photocatalytic performance.

6. Summary and Outlook

This review focus on recent developments related to the treatment of wastewater by BC-based photocatalysts. Various synthesis processes, photocatalytic enhancement mechanisms, and different applications of BCPs were summarized. Semiconductors can be coupled with BC via sol-gel,

hydrothermal/solvothermal, ultrasound, calcination, and in situ methods. Besides the well-known adsorption effects of BC, it can also narrow the band gap, facilitate the electron transport, suppress the electron-hole charges recombination and reduce the photocorrosion of semiconductor, etc. Moreover, examples for the applications of BCPs were also summarized, including TiO₂-BCPs, g-C₃N₄-BCPs, Bismuth-BCPs, and CQD-BCPs, etc.

Despite the exciting development of BCPs, some knowledge gaps and issues still exist.

- Most research on the photocatalytic treatment of wastewater through BCPs focused on individual organic or inorganic substance. However, the real wastewater often contains multicomponent of pollutants. There might be competitive adsorption or photocatalysis between different materials during the removal process. Therefore, the performance of BCPs in treating real wastewater needs to be studied further.
- Recycling significantly reduces the cost of photocatalysis. The reuse of the BCPs from the slurry systems remains a problem, which limits the widespread of their applications. One promising approach to solve this problem is the magnetic separation by applying an external magnetic field in the water treatment process. More research is required to establish the efficient BCPs recovery at large scale.
- Despite its advantages, certain hazardous waste biomass such as sewage sludge and municipal waste could release toxic organic or inorganic substances during the pyrolysis process, thus inducing ecological and health risks. Further research on the assessment of the long-term effects and security of the applications in wastewater treatment needs to be considered.
- By now, most of the research has been carried out in the static system, which is usually applied to test the photocatalytic performance of new catalysts. However, photocatalysis in dynamic conditions may exhibit different abilities. Further investigations are required for the development of BCPs in dynamic photocatalysis system.

Author Contributions: J.C. (Jiali Cui) designed the concept and wrote the first draft of the manuscript. Y.R. and X.Y. contributed with the literature search and illustrations. F.Z., H.L. and J.C. (Jianguo Cui) revised the manuscript. All authors have read and agreed to the published version of the manuscript.

Funding: The authors acknowledge financial support from the Natural Science Foundation of Shanxi (Grant No. 201801D121275), and the Key Research and Development Project of Shanxi (Social Development) (Grant No. 201803D31046).

Conflicts of Interest: The authors declare no conflict of interest.

References

1. Mian, M.M.; Liu, G. Recent progress in biochar-supported photocatalysts: Synthesis, role of biochar, and applications. *RSC Adv.* **2018**, *8*, 14237–14248. [[CrossRef](#)]
2. Shaban, Y.A.; El Maradny, A.A.; Al Farawati, R.K. Photocatalytic reduction of nitrate in seawater using C/TiO₂ nanoparticles. *J. Photochem. Photobiol. A Chem.* **2016**, *328*, 114–121. [[CrossRef](#)]
3. Choi, J.; Park, H.; Hoffmann, M.R. Effects of single metal-ion doping on the visible-light photoreactivity of TiO₂. *J. Phys. Chem. C* **2009**, *114*, 783–792. [[CrossRef](#)]
4. Zhang, Y.; Zhao, Z.; Chen, J.; Cheng, L.; Chang, J.; Sheng, W.; Hu, C.; Cao, S. C-doped hollow TiO₂ spheres: In situ synthesis, controlled shell thickness, and superior visible-light photocatalytic activity. *Appl. Catal. B Environ.* **2015**, *165*, 715–722. [[CrossRef](#)]
5. Asahi, R.; Morikawa, T.; Ohwaki, T.; Aoki, K.; Taga, Y. Visible-light photocatalysis in nitrogen-doped titanium oxides. *Science* **2001**, *293*, 269–271. [[CrossRef](#)] [[PubMed](#)]
6. Devi, L.G.; Kavitha, R. A review on non metal ion doped titania for the photocatalytic degradation of organic pollutants under UV/solar light: Role of photogenerated charge carrier dynamics in enhancing the activity. *Appl. Catal. B Environ.* **2013**, *140*, 559–587. [[CrossRef](#)]
7. Devi, L.G.; Kavitha, R. Review on modified N-TiO₂ for green energy applications under UV/visible light: Selected results and reaction mechanisms. *RSC Adv.* **2014**, *4*, 28265–28299. [[CrossRef](#)]

8. Leary, R.; Westwood, A. Carbonaceous nanomaterials for the enhancement of TiO₂ photocatalysis. *Carbon* **2011**, *49*, 741–772. [[CrossRef](#)]
9. Devi, L.G.; Kavitha, R. Enhanced photocatalytic activity of sulfur doped TiO₂ for the decomposition of phenol: A new insight into the bulk and surface modification. *Mater. Chem. Phys.* **2014**, *143*, 1300–1308. [[CrossRef](#)]
10. Eslami, A.; Amini, M.M.; Yazdanbakhsh, A.R.; Mohseni-Bandpei, A.; Safari, A.A.; Asadi, A. N, S co-doped TiO₂ nanoparticles and nanosheets in simulated solar light for photocatalytic degradation of non-steroidal anti-inflammatory drugs in water: A comparative study. *J. Chem. Technol. Biotechnol.* **2016**, *91*, 2693–2704. [[CrossRef](#)]
11. Li, H.; Hao, Y.; Lu, H.; Liang, L.; Wang, Y.; Qiu, J.; Shi, X.; Wang, Y.; Yao, J. A systematic study on visible-light N-doped TiO₂ photocatalyst obtained from ethylenediamine by sol–gel method. *Appl. Surf. Sci.* **2015**, *344*, 112–118. [[CrossRef](#)]
12. Giannakas, A.; Antonopoulou, M.; Daikopoulos, C.; Deligiannakis, Y.; Konstantinou, I. Characterization and catalytic performance of B-doped, B–N co-doped and B–N–F tri-doped TiO₂ towards simultaneous Cr (VI) reduction and benzoic acid oxidation. *Appl. Catal. B Environ.* **2016**, *184*, 44–54. [[CrossRef](#)]
13. Samsudin, E.M.; Hamid, S.B.A.; Juan, J.C.; Basirun, W.J.; Kandjani, A.E.; Bhargava, S.K. Effective role of trifluoroacetic acid (TFA) to enhance the photocatalytic activity of F-doped TiO₂ prepared by modified sol–gel method. *Appl. Surf. Sci.* **2016**, *365*, 57–68. [[CrossRef](#)]
14. Samsudin, E.M.; Hamid, S.B.A.; Juan, J.C.; Basirun, W.J.; Centi, G. Synergetic effects in novel hydrogenated F-doped TiO₂ photocatalysts. *Appl. Surf. Sci.* **2016**, *370*, 380–393. [[CrossRef](#)]
15. Mendiola-Alvarez, S.; Hernández-Ramírez, A.; Guzmán-Mar, J.; Maya-Treviño, M.; Caballero-Quintero, A.; Hinojosa-Reyes, L. A novel P-doped Fe₂O₃-TiO₂ mixed oxide: Synthesis, characterization and photocatalytic activity under visible radiation. *Catal. Today* **2019**, *328*, 91–98. [[CrossRef](#)]
16. Lai, Y.-K.; Huang, J.-Y.; Zhang, H.-F.; Subramaniam, V.-P.; Tang, Y.-X.; Gong, D.-G.; Sundar, L.; Sun, L.; Chen, Z.; Lin, C.-J. Nitrogen-doped TiO₂ nanotube array films with enhanced photocatalytic activity under various light sources. *J. Hazard. Mater.* **2010**, *184*, 855–863. [[CrossRef](#)]
17. Jyothi, M.; Nayak, V.; Reddy, K.R.; Naveen, S.; Raghu, A. Non-metal (Oxygen, Sulphur, Nitrogen, Boron and Phosphorus)-Doped Metal Oxide Hybrid Nanostructures as Highly Efficient Photocatalysts for Water Treatment and Hydrogen Generation. In *Nanophotocatalysis and Environmental Applications*; Springer: Berlin/Heidelberg, Germany, 2019; pp. 83–105.
18. Khan, S.U.M.; Al-Shahry, M.; Ingler, W.B. Efficient Photochemical Water Splitting by a Chemically Modified n-TiO₂. *Science* **2002**, *297*, 2243–2245. [[CrossRef](#)]
19. Sakthivel, S.; Kisch, H. Daylight Photocatalysis by Carbon-Modified Titanium Dioxide. *Angew. Chem. Int. Ed.* **2003**, *42*, 4908–4911. [[CrossRef](#)]
20. Chen, D.; Jiang, Z.; Geng, J.; Wang, Q.; Yang, D. Carbon and Nitrogen Co-doped TiO₂ with Enhanced Visible-Light Photocatalytic Activity. *Ind. Eng. Chem. Res.* **2007**, *46*, 2741–2746. [[CrossRef](#)]
21. Wang, H.; Lewis, J.P. Effects of dopant states on photoactivity in carbon-doped TiO₂. *J. Phys. Condens. Matter* **2005**, *17*, L209. [[CrossRef](#)]
22. Colmenares, J.C.; Varma, R.S.; Lisowski, P. Sustainable hybrid photocatalysts: titania immobilized on carbon materials derived from renewable and biodegradable resources. *Green Chem.* **2016**, *18*, 5736–5750. [[CrossRef](#)]
23. Luo, M.; Lin, H.; Li, B.; Dong, Y.; He, Y.; Wang, L. A novel modification of lignin on corn-cob-based biochar to enhance removal of cadmium from water. *Bioresour. Technol.* **2018**, *259*, 312–318. [[CrossRef](#)] [[PubMed](#)]
24. Li, H.; Dong, X.; Da Silva, E.B.; De Oliveira, L.M.; Chen, Y.; Ma, L.Q. Mechanisms of metal sorption by biochars: biochar characteristics and modifications. *Chemosphere* **2017**, *178*, 466–478. [[CrossRef](#)] [[PubMed](#)]
25. Lee, D.-J.; Cheng, Y.-L.; Wong, R.-J.; Wang, X.-D. Adsorption removal of natural organic matters in waters using biochar. *Bioresour. Technol.* **2018**, *260*, 413–416. [[CrossRef](#)]
26. Fang, G.; Liu, C.; Gao, J.; Dionysiou, D.D.; Zhou, D. Manipulation of persistent free radicals in biochar to activate persulfate for contaminant degradation. *Environ. Sci. Technol.* **2015**, *49*, 5645–5653. [[CrossRef](#)]
27. Tan, X.; Liu, Y.; Zeng, G.; Wang, X.; Hu, X.; Gu, Y.; Yang, Z. Application of biochar for the removal of pollutants from aqueous solutions. *Chemosphere* **2015**, *125*, 70–85. [[CrossRef](#)]
28. Zhang, S.; Lu, X. Treatment of wastewater containing Reactive Brilliant Blue KN-R using TiO₂/BC composite as heterogeneous photocatalyst and adsorbent. *Chemosphere* **2018**, *206*, 777–783. [[CrossRef](#)]

29. Silvestri, S.; Gonçalves, M.G.; Da Silva Veiga, P.A.; Matos, T.T.D.S.; Peralta-Zamora, P.; Mangrich, A.S. TiO₂ supported on *Salvinia molesta* biochar for heterogeneous photocatalytic degradation of Acid Orange 7 dye. *J. Environ. Chem. Eng.* **2019**, *7*, 102879. [[CrossRef](#)]
30. Zhang, H.; Wang, Z.; Li, R.; Guo, J.; Li, Y.; Zhu, J.; Xie, X. TiO₂ supported on reed straw biochar as an adsorptive and photocatalytic composite for the efficient degradation of sulfamethoxazole in aqueous matrices. *Chemosphere* **2017**, *185*, 351–360. [[CrossRef](#)]
31. Cai, X.; Li, J.; Liu, Y.; Yan, Z.; Tan, X.; Liu, S.; Zeng, G.; Gu, Y.; Hu, X.; Jiang, L. Titanium dioxide-coated biochar composites as adsorptive and photocatalytic degradation materials for the removal of aqueous organic pollutants. *J. Chem. Technol. Biotechnol.* **2018**, *93*, 783–791. [[CrossRef](#)]
32. Kim, J.R.; Kan, E. Heterogeneous photocatalytic degradation of sulfamethoxazole in water using a biochar-supported TiO₂ photocatalyst. *J. Environ. Manag.* **2016**, *180*, 94–101. [[CrossRef](#)]
33. Khataee, A.; Kayan, B.; Gholami, P.; Kalderis, D.; Akay, S. Sonocatalytic degradation of an anthraquinone dye using TiO₂-biochar nanocomposite. *Ultrason. Sonochem.* **2017**, *39*, 120–128. [[CrossRef](#)] [[PubMed](#)]
34. Wang, B.; Liu, B.; Ji, X.-X.; Ma, M.-G. Synthesis, characterization, and photocatalytic properties of bamboo charcoal/TiO₂ composites using four sizes powder. *Materials* **2018**, *11*, 670. [[CrossRef](#)] [[PubMed](#)]
35. Men, Q.; Wang, T.; Ma, C.; Yang, L.; Liu, Y.; Huo, P.; Yan, Y. In-suit preparation of CdSe quantum dots/porous channel biochar for improving photocatalytic activity for degradation of tetracycline. *J. Taiwan Inst. Chem. Eng.* **2019**, *99*, 180–192. [[CrossRef](#)]
36. Vinayagam, M.; Ramachandran, S.; Ramya, V.; Sivasamy, A. Photocatalytic degradation of orange G dye using ZnO/biomass activated carbon nanocomposite. *J. Environ. Chem. Eng.* **2018**, *6*, 3726–3734. [[CrossRef](#)]
37. Kumar, A.; Kumar, A.; Sharma, G.; Naushad, M.; Stadler, F.J.; Ghfar, A.A.; Dhiman, P.; Saini, R.V. Sustainable nano-hybrids of magnetic biochar supported g-C₃N₄/FeVO₄ for solar powered degradation of noxious pollutants- Synergism of adsorption, photocatalysis & photo-ozonation. *J. Clean. Prod.* **2017**, *165*, 431–451.
38. Gao, N.; Lu, Z.; Zhao, X.; Zhu, Z.; Wang, Y.; Wang, D.; Hua, Z.; Li, C.; Huo, P.; Song, M. Enhanced photocatalytic activity of a double conductive C/Fe₃O₄/Bi₂O₃ composite photocatalyst based on biomass. *Chem. Eng. J.* **2016**, *304*, 351–361. [[CrossRef](#)]
39. Lu, L.; Shan, R.; Shi, Y.; Wang, S.; Yuan, H. A novel TiO₂/biochar composite catalysts for photocatalytic degradation of methyl orange. *Chemosphere* **2019**, *222*, 391–398. [[CrossRef](#)]
40. Djellabi, R.; Yang, B.; Wang, Y.; Cui, X.; Zhao, X. Carbonaceous biomass-titania composites with TiOC bonding bridge for efficient photocatalytic reduction of Cr (VI) under narrow visible light. *Chem. Eng. J.* **2019**, *366*, 172–180. [[CrossRef](#)]
41. Lisowski, P.; Colmenares, J.C.; Mašek, O.; Lisowski, W.; Lisovytskiy, D.; Kamińska, A.; Łomot, D. Dual Functionality of TiO₂/Biochar Hybrid Materials: Photocatalytic Phenol Degradation in the Liquid Phase and Selective Oxidation of Methanol in the Gas Phase. *ACS Sustain. Chem. Eng.* **2017**, *5*, 6274–6287. [[CrossRef](#)]
42. Matos, J. Eco-friendly heterogeneous photocatalysis on biochar-based materials under solar irradiation. *Top. Catal.* **2016**, *59*, 394–402. [[CrossRef](#)]
43. Xue, H.; Chen, Y.; Liu, X.; Qian, Q.; Luo, Y.; Cui, M.; Chen, Y.; Yang, D.-P.; Chen, Q. Visible light-assisted efficient degradation of dye pollutants with biomass-supported TiO₂ hybrids. *Mater. Sci. Eng. C* **2018**, *82*, 197–203. [[CrossRef](#)]
44. Xie, X.; Li, S.; Zhang, H.; Wang, Z.; Huang, H. Promoting charge separation of biochar-based Zn-TiO₂/pBC in the presence of ZnO for efficient sulfamethoxazole photodegradation under visible light irradiation. *Sci. Total Environ.* **2019**, *659*, 529–539. [[CrossRef](#)]
45. Kumar, A.; Kumar, A.; Sharma, G.; Al-Muhtaseb, A.A.H.; Naushad, M.; Ghfar, A.A.; Guo, C.; Stadler, F.J. Biochar-templated g-C₃N₄/Bi₂O₂CO₃/CoFe₂O₄ nano-assembly for visible and solar assisted photo-degradation of paraquat, nitrophenol reduction and CO₂ conversion. *Chem. Eng. J.* **2018**, *339*, 393–410. [[CrossRef](#)]
46. Donar, Y.O.; Bilge, S.; Sinağ, A.; Pliekhov, O. TiO₂/Carbon Materials Derived from Hydrothermal Carbonization of Waste Biomass: A Highly Efficient, Low-Cost Visible-Light-Driven Photocatalyst. *ChemCatChem* **2018**, *10*, 1134–1139. [[CrossRef](#)]
47. Peñas-Garzón, M.; Gómez-Avilés, A.; Bedia, J.; Rodríguez, J.J.; Belver, C. Effect of Activating Agent on the Properties of TiO₂/Activated Carbon Heterostructures for Solar Photocatalytic Degradation of Acetaminophen. *Materials* **2019**, *12*, 378. [[CrossRef](#)]

48. Wang, T.; Liu, S.; Mao, W.; Bai, Y.; Chiang, K.; Shah, K.; Paz-Ferreiro, J. Novel Bi₂WO₆ loaded N-biochar composites with enhanced photocatalytic degradation of rhodamine B and Cr (VI). *J. Hazard. Mater.* **2019**. [[CrossRef](#)]
49. Gholami, P.; Khataee, A.; Soltani, R.D.C.; Dinpazhoh, L.; Bhatnagar, A. Photocatalytic degradation of gemifloxacin antibiotic using Zn-Co-LDH@biochar nanocomposite. *J. Hazard. Mater.* **2020**, *382*, 121070. [[CrossRef](#)]
50. Ye, S.; Yan, M.; Tan, X.; Liang, J.; Zeng, G.; Wu, H.; Song, B.; Zhou, C.; Yang, Y.; Wang, H. Facile assembled biochar-based nanocomposite with improved graphitization for efficient photocatalytic activity driven by visible light. *Appl. Catal. B Environ.* **2019**, *250*, 78–88. [[CrossRef](#)]
51. Li, M.; Huang, H.; Yu, S.; Tian, N.; Dong, F.; Du, X.; Zhang, Y. Simultaneously promoting charge separation and photoabsorption of BiOX (X= Cl, Br) for efficient visible-light photocatalysis and photosensitization by compositing low-cost biochar. *Appl. Surf. Sci.* **2016**, *386*, 285–295. [[CrossRef](#)]
52. Liu, M.Y.; Zheng, Y.F.; Song, X.C. Biomass Assisted Synthesis of 3D Hierarchical Structure BiOX (X Cl, Br)-(CMC) with Enhanced Photocatalytic Activity. *J. Nanosci. Nanotechnol.* **2019**, *19*, 5287–5294. [[CrossRef](#)] [[PubMed](#)]
53. Cai, F.-Y.; Zhang, Y.-Q.; Wang, J.-T.; Zhou, J.-R.; Cao, H.-L.; Lü, J. Mixed phase nano-CdS supported on activated biomass carbon as efficient visible light-driven photocatalysts. *Environ. Sci. Pollut. Res.* **2019**, *26*, 31055–31061. [[CrossRef](#)] [[PubMed](#)]
54. Lisowski, P.; Colmenares, J.C.; Mašek, O.; Lisowski, W.; Lisovytskiy, D.; Grzonka, J.; Kurzydłowski, K. Design and Fabrication of TiO₂/Lignocellulosic Carbon Materials: Relevance of Low-temperature Sonocrystallization to Photocatalysts Performance. *ChemCatChem* **2018**, *10*, 3469–3480. [[CrossRef](#)]
55. Peng, X.; Wang, M.; Hu, F.; Qiu, F.; Dai, H.; Cao, Z. Facile fabrication of hollow biochar carbon-doped TiO₂/CuO composites for the photocatalytic degradation of ammonia nitrogen from aqueous solution. *J. Alloys Compd.* **2019**, *770*, 1055–1063. [[CrossRef](#)]
56. Huang, H.-B.; Wang, Y.; Jiao, W.-B.; Cai, F.-Y.; Shen, M.; Zhou, S.-G.; Cao, H.-L.; Lü, J.; Cao, R. Lotus-Leaf-Derived Activated-Carbon-Supported Nano-CdS as Energy-Efficient Photocatalysts under Visible Irradiation. *ACS Sustain. Chem. Eng.* **2018**, *6*, 7871–7879. [[CrossRef](#)]
57. Li, K.; Huang, Z.; Zhu, S.; Luo, S.; Yan, L.; Dai, Y.; Guo, Y.; Yang, Y. Removal of Cr(VI) from water by a biochar-coupled g-C₃N₄ nanosheets composite and performance of a recycled photocatalyst in single and combined pollution systems. *Appl. Catal. B Environ.* **2019**, *243*, 386–396. [[CrossRef](#)]
58. Cruz, G.J.F.; Gómez, M.M.; Solis, J.L.; Rimaycuna, J.; Solis, R.L.; Cruz, J.F.; Rathnayake, B.; Keiski, R.L. Composites of ZnO nanoparticles and biomass based activated carbon: adsorption, photocatalytic and antibacterial capacities. *Water Sci. Technol.* **2018**, *2017*, 492–508. [[CrossRef](#)]
59. Zhai, Y.; Dai, Y.; Guo, J.; Zhou, L.; Chen, M.; Yang, H.; Peng, L. Novel biochar@CoFe₂O₄/Ag₃PO₄ photocatalysts for highly efficient degradation of bisphenol a under visible-light irradiation. *J. Colloid Interface Sci.* **2020**, *560*, 111–121. [[CrossRef](#)]
60. Kumar, A.; Sharma, G.; Naushad, M.; Kumar, A.; Kalia, S.; Guo, C.; Mola, G.T. Facile hetero-assembly of superparamagnetic Fe₃O₄/BiVO₄ stacked on biochar for solar photo-degradation of methyl paraben and pesticide removal from soil. *J. Photochem. Photobiol. A Chem.* **2017**, *337*, 118–131. [[CrossRef](#)]
61. Kumar, A.; Sharma, G.; Naushad, M.; Al-Muhtaseb, A.A.H.; Kumar, A.; Hira, I.; Ahmad, T.; Ghfar, A.A.; Stadler, F.J. Visible photodegradation of ibuprofen and 2,4-D in simulated waste water using sustainable metal free-hybrids based on carbon nitride and biochar. *J. Environ. Manag.* **2019**, *231*, 1164–1175. [[CrossRef](#)]
62. Lisowski, P.; Colmenares, J.C.; Mašek, O.; Łomot, D.; Chernyayeva, O.; Lisovytskiy, D. Novel biomass-derived hybrid TiO₂/carbon material using tar-derived secondary char to improve TiO₂ bonding to carbon matrix. *J. Anal. Appl. Pyrolysis* **2018**, *131*, 35–41. [[CrossRef](#)]
63. Fazal, T.; Razzaq, A.; Javed, F.; Hafeez, A.; Rashid, N.; Amjad, U.S.; Rehman, M.S.U.; Faisal, A.; Rehman, F. Integrating adsorption and photocatalysis: A cost effective strategy for textile wastewater treatment using hybrid biochar-TiO₂ composite. *J. Hazard. Mater.* **2019**. [[CrossRef](#)]
64. Zhu, N.; Li, C.; Bu, L.; Tang, C.; Wang, S.; Duan, P.; Yao, L.; Tang, J.; Dionysiou, D.D.; Wu, Y. Bismuth impregnated biochar for efficient estrone degradation: The synergistic effect between biochar and Bi/Bi₂O₃ for a high photocatalytic performance. *J. Hazard. Mater.* **2020**, *384*, 121258. [[CrossRef](#)]

65. Mamaghani, A.H.; Haghghat, F.; Lee, C.-S. Hydrothermal/solvothermal synthesis and treatment of TiO₂ for photocatalytic degradation of air pollutants: Preparation, characterization, properties, and performance. *Chemosphere* **2019**, *219*, 804–825. [[CrossRef](#)]
66. Lisowski, P.; Colmenares, J.C.; Łomot, D.; Chernyayeva, O.; Lisovytskiy, D. Preparation by sonophotodeposition method of bimetallic photocatalysts Pd–Cu/TiO₂ for sustainable gaseous selective oxidation of methanol to methyl formate. *J. Mol. Catal. A Chem.* **2016**, *411*, 247–256. [[CrossRef](#)]
67. Brandes, R.; Trindade, E.C.A.; Vanin, D.F.; Vargas, V.M.M.; Carminatti, C.A.; Al-Qureshi, H.A.; Recouvreux, D.O.S. Spherical Bacterial Cellulose/TiO₂ Nanocomposite with Potential Application in Contaminants Removal from Wastewater by Photocatalysis. *Fibers Polym.* **2018**, *19*, 1861–1868. [[CrossRef](#)]
68. Zhao, B.; O'connor, D.; Zhang, J.; Peng, T.; Shen, Z.; Tsang, D.C.W.; Hou, D. Effect of pyrolysis temperature, heating rate, and residence time on rapeseed stem derived biochar. *J. Clean. Prod.* **2018**, *174*, 977–987. [[CrossRef](#)]
69. Abdul, G.; Zhu, X.; Chen, B. Structural characteristics of biochar-graphene nanosheet composites and their adsorption performance for phthalic acid esters. *Chem. Eng. J.* **2017**, *319*, 9–20. [[CrossRef](#)]
70. Xiao, X.; Chen, B. A direct observation of the fine aromatic clusters and molecular structures of biochars. *Environ. Sci. Technol.* **2017**, *51*, 5473–5482. [[CrossRef](#)]
71. Fan, S.; Wang, Y.; Wang, Z.; Tang, J.; Tang, J.; Li, X. Removal of methylene blue from aqueous solution by sewage sludge-derived biochar: Adsorption kinetics, equilibrium, thermodynamics and mechanism. *J. Environ. Chem. Eng.* **2017**, *5*, 601–611. [[CrossRef](#)]
72. Zheng, Y.; Yang, Y.; Zhang, Y.; Zou, W.; Luo, Y.; Dong, L.; Gao, B. Facile one-step synthesis of graphitic carbon nitride-modified biochar for the removal of reactive red 120 through adsorption and photocatalytic degradation. *Biochar* **2019**, *1*, 89–96. [[CrossRef](#)]
73. Geng, A.; Meng, L.; Han, J.; Zhong, Q.; Li, M.; Han, S.; Mei, C.; Xu, L.; Tan, L.; Gan, L. Highly efficient visible-light photocatalyst based on cellulose derived carbon nanofiber/BiOBr composites. *Cellulose* **2018**, *25*, 4133–4144. [[CrossRef](#)]
74. Ren, W.; Ai, Z.; Jia, F.; Zhang, L.; Fan, X.; Zou, Z. Low temperature preparation and visible light photocatalytic activity of mesoporous carbon-doped crystalline TiO₂. *Appl. Catal. B Environ.* **2007**, *69*, 138–144. [[CrossRef](#)]
75. Al-Kahtani, A.A.; Alshehri, S.M.; Naushad, M.; Ruksana; Ahamad, T. Fabrication of highly porous N/S doped carbon embedded with ZnS as highly efficient photocatalyst for degradation of bisphenol. *Int. J. Biol. Macromol.* **2019**, *121*, 415–423. [[CrossRef](#)] [[PubMed](#)]
76. Wong, J.W.C.; Webber, J.B.W.; Ogbonnaya, U.O. Characteristics of biochar porosity by NMR and study of ammonium ion adsorption. *J. Anal. Appl. Pyrolysis* **2019**, *143*, 104687. [[CrossRef](#)]
77. Zhong, Y.; Deng, Q.; Zhang, P.; Wang, J.; Wang, R.; Zeng, Z.; Deng, S. Sulfonic acid functionalized hydrophobic mesoporous biochar: Design, preparation and acid-catalytic properties. *Fuel* **2019**, *240*, 270–277. [[CrossRef](#)]
78. Jiang, Y.; Ren, C.; Guo, H.; Guo, M.; Li, W. Speciation Transformation of Phosphorus in Poultry Litter during Pyrolysis: Insights from XRD, FTIR, and Solid-state NMR Spectroscopy. *Environ. Sci. Technol.* **2019**, *53*, 13841–13849. [[CrossRef](#)]
79. Igalavithana, A.D.; Mandal, S.; Niazi, N.K.; Vithanage, M.; Parikh, S.J.; Mukome, F.N.; Rizwan, M.; Oleszczuk, P.; Al-Wabel, M.; Bolan, N. Advances and future directions of biochar characterization methods and applications. *Crit. Rev. Environ. Sci. Technol.* **2017**, *47*, 2275–2330. [[CrossRef](#)]
80. Yao, X.; Ma, C.; Huang, H.; Zhu, Z.; Dong, H.; Li, C.; Zhang, W.; Yan, Y.; Liu, Y. Solvothermal-Assisted Synthesis of Biomass Carbon Quantum Dots/Bismuth Oxyiodide Microflower for Enhanced Photocatalytic Activity. *Nano* **2018**, *13*, 1850031. [[CrossRef](#)]
81. Xiong, X.; Yu, I.K.M.; Chen, S.S.; Tsang, D.C.W.; Cao, L.; Song, H.; Kwon, E.E.; Ok, Y.S.; Zhang, S.; Poon, C.S. Sulfonated biochar as acid catalyst for sugar hydrolysis and dehydration. *Catal. Today* **2018**, *314*, 52–61. [[CrossRef](#)]
82. Zou, W.; Gao, B.; Ok, Y.S.; Dong, L. Integrated adsorption and photocatalytic degradation of volatile organic compounds (VOCs) using carbon-based nanocomposites: A critical review. *Chemosphere* **2019**, *218*, 845–859. [[CrossRef](#)] [[PubMed](#)]
83. Di Valentin, C.; Pacchioni, G.; Selloni, A. Theory of carbon doping of titanium dioxide. *Chem. Mater.* **2005**, *17*, 6656–6665. [[CrossRef](#)]
84. Yin, G.; Wang, Y.; Yuan, Q. Ti³⁺-doped TiO₂ hollow sphere with mixed phases of anatase and rutile prepared by dual-frequency atmospheric pressure plasma jet. *J. Nanopart. Res.* **2018**, *20*, 208. [[CrossRef](#)]

85. Low, F.W.; Lai, C.W.; Hamid, S.B.A. Surface modification of reduced graphene oxide film by Ti ion implantation technique for high dye-sensitized solar cells performance. *Ceram. Int.* **2017**, *43*, 625–633. [[CrossRef](#)]
86. Lu, Z.; Zeng, L.; Song, W.; Qin, Z.; Zeng, D.; Xie, C. In situ synthesis of C-TiO₂/g-C₃N₄ heterojunction nanocomposite as highly visible light active photocatalyst originated from effective interfacial charge transfer. *Appl. Catal. B Environ.* **2017**, *202*, 489–499. [[CrossRef](#)]
87. Khalid, N.; Majid, A.; Tahir, M.B.; Niaz, N.; Khalid, S. Carbonaceous-TiO₂ nanomaterials for photocatalytic degradation of pollutants: A review. *Ceram. Int.* **2017**, *43*, 14552–14571. [[CrossRef](#)]
88. Hideyuki, K.; Takahisa, A.; Koichi, Y. Theoretical study of the structure and optical properties of carbon-doped rutile and anatase titanium oxides. *J. Chem. Phys.* **2005**, *123*, 37.
89. Djellabi, R.; Yang, B.; Xiao, K.; Gong, Y.; Cao, D.; Sharif, H.M.A.; Zhao, X.; Zhu, C.; Zhang, J. Unravelling the mechanistic role of TiOC bonding bridge at titania/lignocellulosic biomass interface for Cr (VI) photoreduction under visible light. *J. Colloid Interface Sci.* **2019**, *553*, 409–417. [[CrossRef](#)] [[PubMed](#)]
90. Bao, N.; Li, Y.; Wei, Z.; Yin, G.; Niu, J. Adsorption of dyes on hierarchical mesoporous TiO₂ fibers and its enhanced photocatalytic properties. *J. Phys. Chem. C* **2011**, *115*, 5708–5719. [[CrossRef](#)]
91. Zhu, Z.; Fan, W.; Liu, Z.; Yu, Y.; Dong, H.; Huo, P.; Yan, Y. Fabrication of the metal-free biochar-based graphitic carbon nitride for improved 2-Mercaptobenzothiazole degradation activity. *J. Photochem. Photobiol. A Chem.* **2018**, *358*, 284–293. [[CrossRef](#)]
92. Meng, L.; Yin, W.; Wang, S.; Wu, X.; Hou, J.; Yin, W.; Feng, K.; Ok, Y.S.; Wang, X. Photocatalytic behavior of biochar-modified carbon nitride with enriched visible-light reactivity. *Chemosphere* **2020**, *239*, 124713. [[CrossRef](#)] [[PubMed](#)]
93. Zhao, X.; Lu, Z.; Ji, R.; Zhang, M.; Yi, C.; Yan, Y. Biomass carbon modified Z-scheme g-C₃N₄/Co₃O₄ heterojunction with enhanced visible-light photocatalytic activity. *Catal. Commun.* **2018**, *112*, 49–52. [[CrossRef](#)]
94. Shi, M.; Wei, W.; Jiang, Z.; Han, H.; Gao, J.; Xie, J. Biomass-derived multifunctional TiO₂/carbonaceous aerogel composite as a highly efficient photocatalyst. *RSC Adv.* **2016**, *6*, 25255–25266. [[CrossRef](#)]
95. Fang, G.; Zhu, C.; Dionysiou, D.D.; Gao, J.; Zhou, D. Mechanism of hydroxyl radical generation from biochar suspensions: Implications to diethyl phthalate degradation. *Bioresour. Technol.* **2015**, *176*, 210–217. [[CrossRef](#)]
96. Tan, X.-F.; Liu, Y.-G.; Gu, Y.-L.; Xu, Y.; Zeng, G.-M.; Hu, X.-J.; Liu, S.-B.; Wang, X.; Liu, S.-M.; Li, J. Biochar-based nano-composites for the decontamination of wastewater: A review. *Bioresour. Technol.* **2016**, *212*, 318–333. [[CrossRef](#)]
97. Fang, G.; Liu, C.; Wang, Y.; Dionysiou, D.D.; Zhou, D. Photogeneration of reactive oxygen species from biochar suspension for diethyl phthalate degradation. *Appl. Catal. B Environ.* **2017**, *214*, 34–45. [[CrossRef](#)]
98. Wan, J.; Sun, L.; Fan, J.; Liu, E.; Hu, X.; Tang, C.; Yin, Y. Facile synthesis of porous Ag₃PO₄ nanotubes for enhanced photocatalytic activity under visible light. *Appl. Surf. Sci.* **2015**, *355*, 615–622. [[CrossRef](#)]
99. Jin, J.; Sun, K.; Wang, Z.; Yang, Y.; Han, L.; Xing, B. Characterization and phenanthrene sorption of natural and pyrogenic organic matter fractions. *Environ. Sci. Technol.* **2017**, *51*, 2635–2642. [[CrossRef](#)]
100. Shi, S.; Liu, J.; Xu, J.; Zeng, Q.; Hou, Y.; Jiang, B. Effects of biochar on the phenol treatment performance and microbial communities shift in sequencing batch reactors. *Water Res.* **2019**, *161*, 1–10. [[CrossRef](#)]
101. Dutta, T.; Kwon, E.; Bhattacharya, S.S.; Jeon, B.H.; Deep, A.; Uchimiya, M.; Kim, K.-H. Polycyclic aromatic hydrocarbons and volatile organic compounds in biochar and biochar-amended soil: A review. *Gcb Bioenergy* **2017**, *9*, 990–1004. [[CrossRef](#)]
102. Meng, A.; Zhang, L.; Cheng, B.; Yu, J. Dual Cocatalysts in TiO₂ Photocatalysis. *Adv. Mater.* **2019**, *31*, 1807660. [[CrossRef](#)]
103. Wang, X.; Maeda, K.; Thomas, A.; Takanabe, K.; Xin, G.; Carlsson, J.M.; Domen, K.; Antonietti, M. A metal-free polymeric photocatalyst for hydrogen production from water under visible light. *Nat. Mater.* **2009**, *8*, 76. [[CrossRef](#)]
104. Wen, J.; Xie, J.; Chen, X.; Li, X. A review on g-C₃N₄-based photocatalysts. *Appl. Surf. Sci.* **2017**, *391*, 72–123. [[CrossRef](#)]
105. Kumar, A.; Kumar, A.; Sharma, G.; Ala'a, H.; Naushad, M.; Ghfar, A.A.; Stadler, F.J. Quaternary magnetic BiOCl/g-C₃N₄/Cu₂O/Fe₃O₄ nano-junction for visible light and solar powered degradation of sulfamethoxazole from aqueous environment. *Chem. Eng. J.* **2018**, *334*, 462–478. [[CrossRef](#)]

106. Zhang, L.; Jin, Z.; Huang, S.; Huang, X.; Xu, B.; Hu, L.; Cui, H.; Ruan, S.; Zeng, Y.-J. Bio-inspired carbon doped graphitic carbon nitride with booming photocatalytic hydrogen evolution. *Appl. Catal. B Environ.* **2019**, *246*, 61–71. [[CrossRef](#)]
107. Li, C.; Zhao, G.; Yan, T.; Zhang, T.; Liu, X.; Long, X.; Duan, H.; Jiao, F. Enhanced visible-light-induced photocatalytic performance of Bi₂O₃/ZnAl-LDH-C for dyes removal in water. *Mater. Lett.* **2019**, *244*, 215–218. [[CrossRef](#)]
108. Li, S.; Wang, Z.; Xie, X.; Liang, G.; Cai, X.; Zhang, X.; Wang, Z. Fabrication of vessel-like biochar-based heterojunction photocatalyst Bi₂S₃/BiOBr/BC for diclofenac removal under visible LED light irradiation: Mechanistic investigation and intermediates analysis. *J. Hazard. Mater.* **2019**. [[CrossRef](#)]
109. Li, S.; Wang, Z.; Zhao, X.; Yang, X.; Liang, G.; Xie, X. Insight into enhanced carbamazepine photodegradation over biochar-based magnetic photocatalyst Fe₃O₄/BiOBr/BC under visible LED light irradiation. *Chem. Eng. J.* **2019**, *360*, 600–611. [[CrossRef](#)]
110. Briscoe, J.; Marinovic, A.; Sevilla, M.; Dunn, S.; Titirici, M. Biomass-Derived Carbon Quantum Dot Sensitizers for Solid-State Nanostructured Solar Cells. *Angew. Chem. Int. Ed.* **2015**, *54*, 4463–4468. [[CrossRef](#)]
111. Hassan, M.; Gomes, V.G.; Dehghani, A.; Ardekani, S.M. Engineering carbon quantum dots for photomediated theranostics. *Nano Res.* **2018**, *11*, 1–41. [[CrossRef](#)]
112. Zhang, J.; Ma, Y.; Du, Y.; Jiang, H.; Zhou, D.; Dong, S. Carbon nanodots/WO₃ nanorods Z-scheme composites: Remarkably enhanced photocatalytic performance under broad spectrum. *Appl. Catal. B Environ.* **2017**, *209*, 253–264. [[CrossRef](#)]
113. Wang, T.; Liu, X.; Men, Q.; Ma, C.; Liu, Y.; Ma, W.; Liu, Z.; Wei, M.; Li, C.; Yan, Y. Surface plasmon resonance effect of Ag nanoparticles for improving the photocatalytic performance of biochar quantum-dot/Bi₄Ti₃O₁₂ nanosheets. *Chin. J. Catal.* **2019**, *40*, 886–894. [[CrossRef](#)]



© 2020 by the authors. Licensee MDPI, Basel, Switzerland. This article is an open access article distributed under the terms and conditions of the Creative Commons Attribution (CC BY) license (<http://creativecommons.org/licenses/by/4.0/>).